

PROGRESS REPORT 2004

PROJECT TITLE

DETERMINATION OF EFFECTIVE HYDROGEOLOGICAL PARAMETERS USING AN EXPERIMENTAL STRATIGRAPHY

PRINCIPAL INVESTIGATORS

- i. University PI: Mark Person, Indiana University, Department of Geological Sciences, 1001 E 10th St. Bloomington, IN 47405, mperson@indiana.edu
- ii. LANL PI: Carl Gable, EES-6 MS T003, Los Alamos National Laboratory, Los Alamos NM 87545 gable@lanl.gov
- iii. Ye Zhang, Ph.D. candidate, Indiana University, Department of Geological Sciences, 1001 E 10th St. Bloomington, IN 47405

PROJECT OBJECTIVES AND APPROCHES

In this study, a 2D stratigraphic image of a sedimentary deposit is scaled-up to create a synthetic basin-scale hydraulic conductivity map which contains sedimentary heterogeneity at various scales. The use of experimental stratigraphic deposits represents an entirely new approach to study a variety of issues related to conductivity heterogeneity. The overall objective has been three-fold in this study:

- (1) We assess the spatial structure of hydraulic conductivity by constructing experimental $\ln(K)$ variograms for select samples representing deposits created by different depositional processes. The “scale-effect” in $\ln(K)$ correlation range is evaluated. We also attempt to identify the spectral characteristics of the different deposits.
- (2) We conduct flow and transport simulations in the select samples to understand
 - (a) How the effective hydraulic conductivity scales with change of support.
 - (b) How the different conductivity heterogeneity reflecting different sedimentary structures impact solute dispersion.
 - (c) What methods are optimal in estimating the effective hydraulic conductivity and macro-dispersivity.
 - (d) The link between the geostatistical parameters of the deposits with the effective properties: under what conditions does the classic stochastic-analytic theory apply? Can we find a field scale representative elementary volume (FSREV) upon which an effective hydraulic conductivity can be estimated for a stratigraphic unit?

- (3) We conduct flow and transport simulations in the full basin to evaluate the impact of effective parameterization commonly employed to model large-scale flow/transport systems (“layer-cake” models).

SUMMARY OF RESEARCH RESULTS TO DATE

(1) Geostatistical Analysis

The spatial correlation structure of the hydraulic conductivity was analyzed for select deposits (samples) created in different depositional environments (upstream fluvial, shoreline, fluvial/floodplain, turbidite and deepwater) (Fig. 1). Experimental $\ln(K)$ variograms were computed along the statistical axes of each sample and both exponential model and power law model were fitted to obtain integral scales and Hausdorff measure, respectively. We find that in this multi-scale sedimentary system, the shape of the experimental variogram depends on the problem domain size in relation to the size of the local-scale heterogeneity (Fig.2). Stationary correlation structure may occur at separate and distinct scales each corresponding to a particular hierarchy; the integral scale fitted thus becomes dependent on the problem size. Multi-level correlation structure can occur due to statistical mixing at a given scale, while 2-level variograms observed in prior studies may be reinterpreted to identify two disparate scales of local stationarity (Fig. 3). The Hausdorff measure obtained has a comparable range to natural geological deposits and tends to increase for layered deposits (Fig.4). This implies that fractal characteristics may be process-dependent.

(2) Effective Hydrologic Conductivity (K^*):

The effective conductivity of the select deposits was evaluated next with three numerical up-scaling methods, a stochastic-analytic theory and numerical tracer tests. The numerical methods are referred to as Simple Laplacian (SL), Full Tensor Method (FTM), and Periodic Boundary Condition (PBC). The stochastic-analytic theory assumes that the hydraulic conductivity in each deposit is log-normally distributed with stationary, exponential-type correlation structure. The numerical tracer tests are conducted using three different initial tracer plume dimensions to represent a point source (diameter~ a single layer thickness), a line source and a plume. The PBC gives a symmetrical K^* full tensor and is considered the best method among all (all numerical methods are validated by solving for test problems with analytical solutions). The assumptions used for the up-scaling analysis and the subsequent full-basin numerical flow and transport simulations are listed in Table 1. Results of the up-scaling for K^* are summarized in the following

sections (note that the results of the different methods are in general compared against those computed with PBC):

(a) Numerical Methods:

\mathbf{K}^* estimated with different numerical methods are summarized in Table 2. Overall, all three methods give consistent results in \mathbf{K}^* computed: though the S.L. method can not compute the off-diagonal terms, all \mathbf{K}^* computed are diagonally dominated. This is due to the fact that the scale-up of the deposits from the experimental scale to the basin scale has resulted in low incline of the bedding plane. For the deposits analyzed, all 3 methods are almost equally accurate in obtaining the principal components $[K_{\max}, K_{\min}]$ of \mathbf{K}^* (Fig. 5 a, b). The principal components (K_{\max} , K_{\min}) computed with the PBC are further plotted against the Wiener's Bound $[K_H, K_A]$ as well as the geometric mean of the local conductivity (K_G) (Fig. 5 c). Overall, sedimentary layering promotes the principal components of \mathbf{K}^* to approach the Wiener's Bound: $K_{\max} \Rightarrow K_A$; $K_{\min} \Rightarrow K_H$. Without layering, \mathbf{K}^* tends to be isotropic and K_G is a good approximation for the effective hydraulic conductivity. These are consistent with the existing theories in groundwater hydrology for a two-dimensional problem. Similarly, layering enhances \mathbf{K}^* anisotropy: deposits with the anisotropy ratio significantly greater than 1 include the shoreline deposits (samples 1, 5), the fluvial/floodplain deposits (samples 8, 9, 10, 11), and the turbidite (samples 6, 7) (Fig. 5d). Though the principal angles are small (since the beds in the basin are nearly flat), they are sensitive to the presence of faults. For example, the fluvial/floodplain samples 8, 9, 10 have positive principal angles, but that of sample 11 is negative, reflecting the influence of faults. Similarly, the presence of faults in sample 3 has resulted in a more negative principal angle than that of sample 2. In addition, for all samples analyzed, appreciable difference exists between the principal angle and the major statistical axis: for layered deposits (samples 6~11), the major statistical axis is in general greater than the principal angle. Note that the major statistical axis reflects the average bedding angle. This indicates that the bedding plane may determine the statistical axis of the hydraulic conductivity spatial correlation, but it may not determine the principal directions of the effective hydraulic conductivity.

Using the PBC, \mathbf{K}^* is also computed for the fluvial (sample 3), fluvial/floodplain (sample 8), turbidite (sample 6), and the faulted zone (sample 11) for increasing domain size until the full sample size is reached. The principal components of \mathbf{K}^* computed for sample 3, 8, 6 tend to increase with support size and later flatten out after approximately one correlation length (Fig. 6); this asymptotic size may thus define a FSREV and the asymptotic \mathbf{K}^* may define an effective hydraulic conductivity for the stratigraphic unit. For the faulted block (sample 11), the opposite is

true as \mathbf{K}^* computed for the smaller regions are larger and decrease to near constant values. Visual inspection on the conductivity field indicates that the conductivity in the lower portion of this sample has higher sand content; had the select sub regions started from the upper corners with lower sand content, an increasing trend would be expected. Overall, the scale behavior of the conductivity is consistent with the observed data, the difference being that in the upscaling analysis conducted herein, a consistent approach is used to compute \mathbf{K}^* with a single “measurement method”. It’s clear that conductivity heterogeneity is the cause for the scale behavior rather than inconsistency in the measurement method. In addition, a power law function is fitted to obtained a scaling component (m). For the samples analyzed above, there exists a positive correlation between the scaling exponent and $\ln(K)$ variance (σ_f^2) and correlation length: $|m| \sim \sigma_f^2 \lambda_1$

(b) Stochastic-Analytic Method:

The principal components [K_{\max} , K_{\min}] of \mathbf{K}^* can be estimated for all samples using the stochastic-analytic model developed by Gelhar and Axness (1983). Results are listed in Table 2 along with the geostatistical parameters of each sample obtained based on variogram modeling on the same deposits. The percent relative error using the stochastic-analytic model is also computed. In general, the stochastic-analytic model overestimates K_{\max} , but is fairly accurate for the fluvial (sample 2, 3), fluvial/floodplain (sample 8, 9, 10, 11) and the marine deposits (sample 12, 13), e.g., relative error < 5%. These deposits are in general characterized by stationary exponential variograms along the major statistical axis (the non-stationary faulted region is nonetheless dominated by a lateral exponential correlation structure). The stochastic-analytic model tends to underestimate K_{\min} and the relative error becomes quite large, especially for the fluvial/ floodplain deposits, as their minor variograms are non-stationary with multiple correlation ranges and variability levels. However, if a larger scale exponential model is fitted onto the minor variograms of these deposits, the stochastic-analytic model prediction improves greatly (Table 3). Thus, the applicability of the stochastic-analytic theory depends on our ability to determine a prior a *statistical homogeneity* scale for the sample data based on geological insight. In addition, to compare across samples with different variability levels, a scatter plot (Fig. 7) is constructed for the variance of $\ln K$ against $\ln(K_{\max}/K_G)$; the stochastic-analytic model prediction is also plotted for different statistical anisotropy ratio (ρ). Overall, for a given ρ , as σ_f^2 increases, K_{\max} increases from K_G towards K_A ; for a given σ_f^2 , K_{\max} increases as ρ increases.

(c) Numerical Tracer Tests:

For all samples, K_{\max} is inferred based on moment analysis on six different tracer test outcomes for 3 initial tracer dimensions and alternative assumption of without and with local dispersion (Table 4). With the exception of sample 6, the best estimates of K_{\max} come from tracer tests conducted with line and plume sources which were able to sample more of the flow fields. The worst estimates usually come from the point source tracer tests. As the magnitude of K_{\max} increases, the absolute difference between K_{\max} estimated with tracer tests and that estimated with PBC increases (Fig. 8a). The relative error of using tracer tests to estimate K_{\max} is also grouped for samples created in similar depositional environment (Fig. 8b). In general, the tracer test results are most accurate for the fairly homogenous deepwater deposits regardless of the initial plume dimensions and the assumption of local dispersion. For the rest of the deposits containing sedimentary structures, initial plume dimensions and the assumptions of local dispersion affect the accuracy of using tracer tests to estimate K_{\max} ; different sedimentary structure also determines the characteristics of the error. For example, for the fluvial deposits, the non-point-source tracer tests overestimate K_{\max} with the error ranging from 0 to 10%. For the fluvial/floodplain deposits, all tracer tests underestimate K_{\max} with the error ranging from 0 to -10%. The faulted zone (sample 11) is an exception as all tracer tests significantly overestimate K_{\max} . This is due to the presence of a preferential flow pathway near the center of the deposits. For the layered shoreline and turbidite deposits, the tracer tests assuming local dispersion (solid symbols) tend to underestimate K_{\max} compared to the purely advective cases.

(3) Macro-dispersivity (A):

For each sample, moment analysis of the plume covariance is used to compute an *apparent* macro-dispersivity (α_L^M , α_T^M) for the same six tracer tests conducted to estimate K_{\max} . Several observations are listed:

- (a) Regardless of the assumption of local dispersion, α_L^M fluctuates widely around 0.0 in the point-source tracer tests, while it is generally positive in line-source and plume-source tracer tests. (All following discussions are on line/plume source only).
- (b) For the nearly homogenous deposits (sample 2, 12), the initial plume dimensions and the assumption of local dispersion has nearly no impact on α_L^M (Fig. 9, 10); though with local dispersion, the plumes are more mixed internally. No asymptotic behavior is observed even though the sample size is many times the lateral correlation length, contrary to theory prediction.

(c) For layered deposits with $L_x < \lambda_{\max}$ (sample 6, 7), both the initial plume size and local dispersion impacts α_L^M (Fig. 11). Large disparity in mean displacement also exists between the purely advective case and the dispersive case which has a slower mean plume velocity: dispersion causes some of the particles to be trapped in low-conductivity regions. Among all cases, only α_L^M of the advective case of the plume reaches a nearly asymptotic value.

(d) For layered deposits with $L_x > \lambda_{\max}$ (sample 8, 9, 10), local dispersion has nearly no impact on α_L^M (Fig. 12). Pre-asymptotic to asymptotic behavior is also observed, though more fully developed in sample 8 whose lateral size is more extensive than sample 9 and 10. It's of further interest to note that the larger plume gives an asymptotic α_L^M that is 50 m smaller than the line source. Thus larger plumes do not necessarily produce higher lateral dispersion.

(e) For the faulted fluvial/floodplain deposits, hydraulic conductivity is statistically non-stationary, accordingly, asymptotic behavior is not observed. The solute plume migration is dominated by channeling through a preferential flow pathway near the center of the deposits.

(f) In general, α_T^M reaches 0.0 asymptotically, consistent with theory prediction.

Overall, the asymptotic behavior in α_L^M only arises in layered deposits for large scale tracer test.

Depending on the sample size relative to the correlation length, local dispersion may or may not be important to impact solute spreading, though it always enhances solute mixing with a plume.

(4) Full Basin Simulation/Parallel Codes

To simulate groundwater flow and solute transport in the full basin, we used Lagrit (Los Alamos) to generate a numerical grid of 424,217 nodes and 845,208 elements. A fully heterogeneous model represents the complete hydraulic conductivity distribution in the basin; two geological framework models use effective conductivity for each stratigraphic unit for flow simulation and macro-dispersivity for transport simulation (Fig. 14). To solve the large-scale flow and transport problems efficiently, we developed parallel flow and transport codes calling MPI. The parallel codes were first validated by solving for smaller test problems where serial solution exist (Fig. 15). A preliminary basin-scale flow simulation was solved in 40 seconds using 4 processors on an Indiana University Linux PC cluster for the fully heterogeneous model and the hydro-stratigraphic model for which each unit has a \mathbf{K}^* computed with PBC (Fig. 16).

(5) Future Work

- Comparison of α_L^M predicted by different stochastic theories (based on sample $\ln(K)$ geostatistical parameters) with that inferred from the tracer tests. Under what conditions do the theories fail to predict solute dispersion characteristics?
- Using effective K^* in flow calculation, what up-scaling methods (analytical or numerical) results in minimum error in terms of head and velocity distribution in the basin? Do the specified boundary conditions impact our findings?
- In a full-basin transport simulation, the groundwater velocity field is non-stationary. How does this impact solute transport? Can we identify the sedimentary structures that have the largest impact? Can framework models based on macro-dispersivity capture the mean spreading characteristics?

LIST OF PUBLICATIONS

Manuscripts submitted:

- **Zhang Y.**, M. Person, C. Paola, C.W. Gable, X-H. Wen, M.J. Davis, 2004, Geostatistical Analysis of an Experimental Stratigraphy, *submitted* to Water Resources Research, Manuscript # 2004WR003756.

Manuscripts in preparation:

- **Zhang Y.**, M. Person, C.W. Gable, X-H. Wen, 2004, Determination of Effective Hydrologic Parameters Using High Resolution Experimental Stratigraphy.

LIST OF PRESENTATIONS

- 2004 (pending), GSA Annual Meeting, Modeling Flow and Transport in Chemically and Physically Heterogeneous Media, Denver, Colorado.
- 2002, Gordon Research Conference, Flow and Transport in Permeable Media, Andover, Massachusetts
- 2000, SEPM/IAS Research Conference Environmental Sedimentology: Hydrogeology of Sedimentary Aquifers, Santa Fe, New Mexico

NAME OF GRADUATE STUDENT

Ye Zhang, Ph.D. candidate.

PROGRESS TOWARDS PH.D.

Ye Zhang is scheduled to graduate in Spring, 2005.

VISITS TO LOS ALAMOS/TO UNIVERSITY

During both June, 2003 and June 2004, co-PI Mar Person and his doctoral student, Ye Zhang spent a week at Los Alamos National Labs at EES-6 working with Dr. Gable on mesh generation with LaGrit. Person also met with several other individuals to present to discuss their research programs. During April (?), 2003, Dr. Gable has visited Dr. Person and Ye Zhang at Indiana University.

BUDGET

The budget to Indiana University was spent primarily on salaries for Linda Zhang, a post doc (Yongli Gao), and the PI (Person) during the spring and summer months. Person and Zhang worked on developing a two-dimensional representations of solute mass transport using Lagrit. Gao began work on using LaGrit to develop hydrothermal models of fluid flow within idealized representations of the Great Basin. This work is ongoing and we expect to have some preliminary results of this model during the summer of 2005. Details of the Budget are provided below. A paper based on Zhang, Person, and Gables work was recently submitted to Water Resources Research.

Individual	Cost	Item	Effort
Zhang	\$8,375	stipend	spring 04
Zhang	\$544	health care	
	\$2,039	travel	
	\$500	supplies	
Gao	\$6,250	post doc	2.5 months
Gao	\$2,331	fringe fee	2.5 months
	2780.5	remission summer	
Person	5600	Salary	2 weeks
Person	1160	fringe	
Total	\$29,579		

EFFORTS TO SECURE FUTURE FUNDING

Person and Zhang are working with Carl Gable to develop a DOE proposal to the fossil fuels program to support and extension of the work to date. This would focus on conducting tracer tests with the Jurassic Tank deposits prior to dissection and then developing three-dimensional models of the tank sediments. The work has broad application to upscaling studies in the petroleum industry.

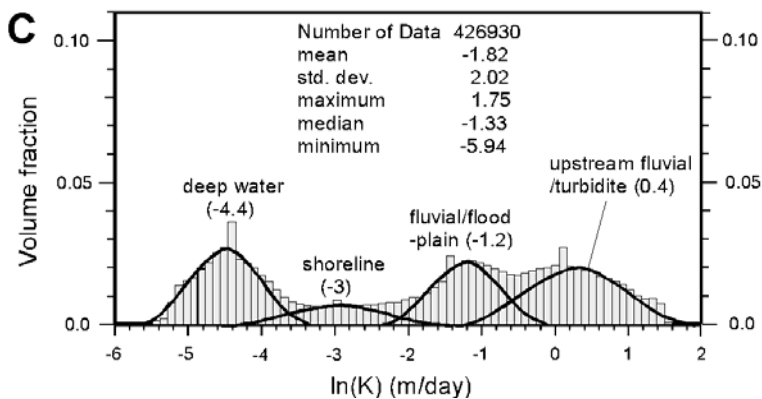
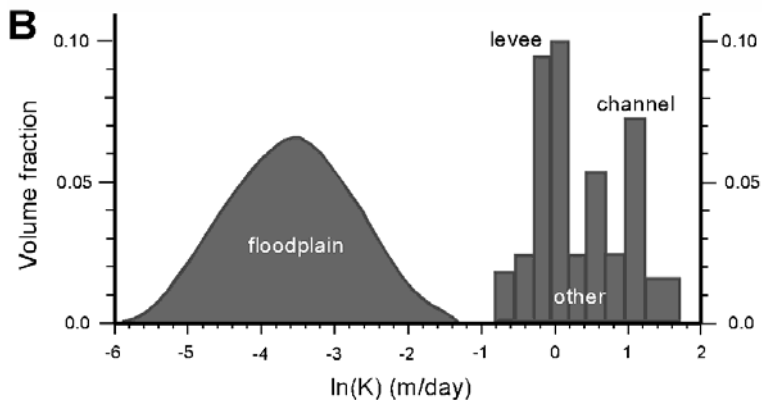
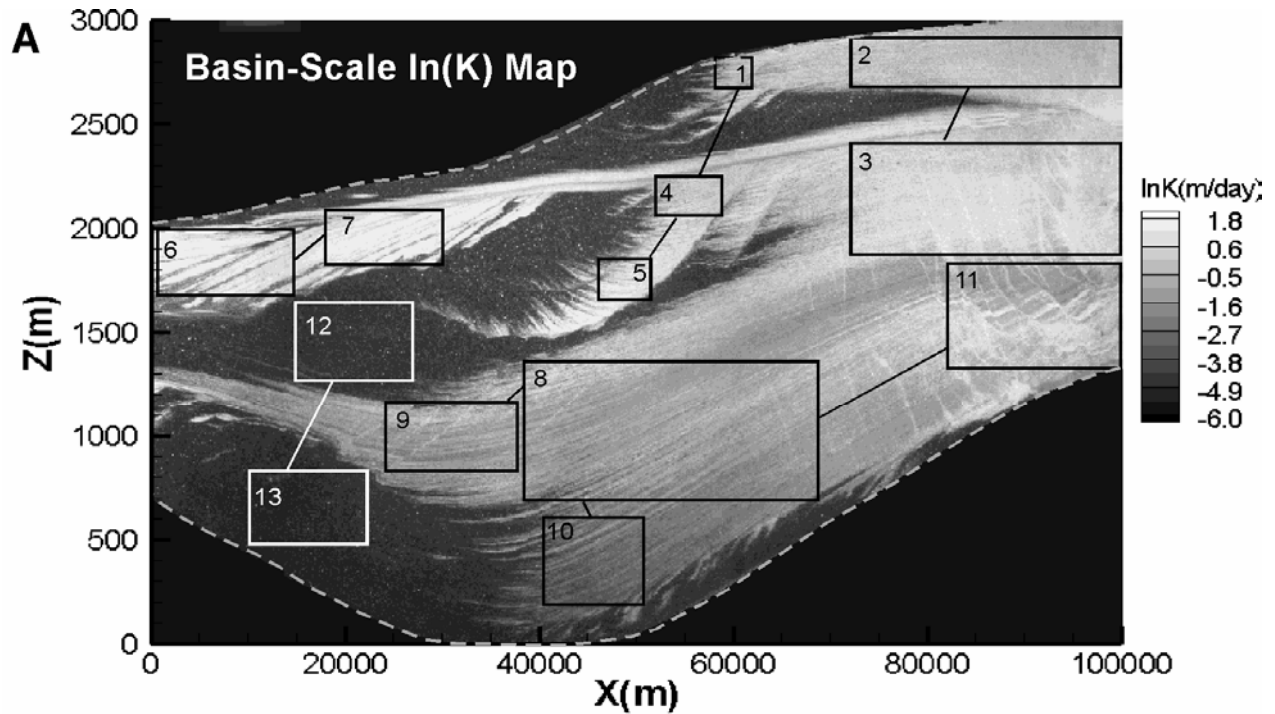


Figure 1. (A) An interpolated basin-scale $\ln(K)$ map (in m/day) used in this study. Location of the deposits analyzed is indicated as well as the sample ID. Deposits created in similar depositional environment are linked by lines. (B) $\ln(K)$ (m/day) frequency distribution based on measurements from an alluvial fan deposit in Livermore Valley, California (after Lu et al., 2002). (C) $\ln(K)$ frequency distribution of (A). Four log-normal populations were identified, superimposed with four normal density curves.

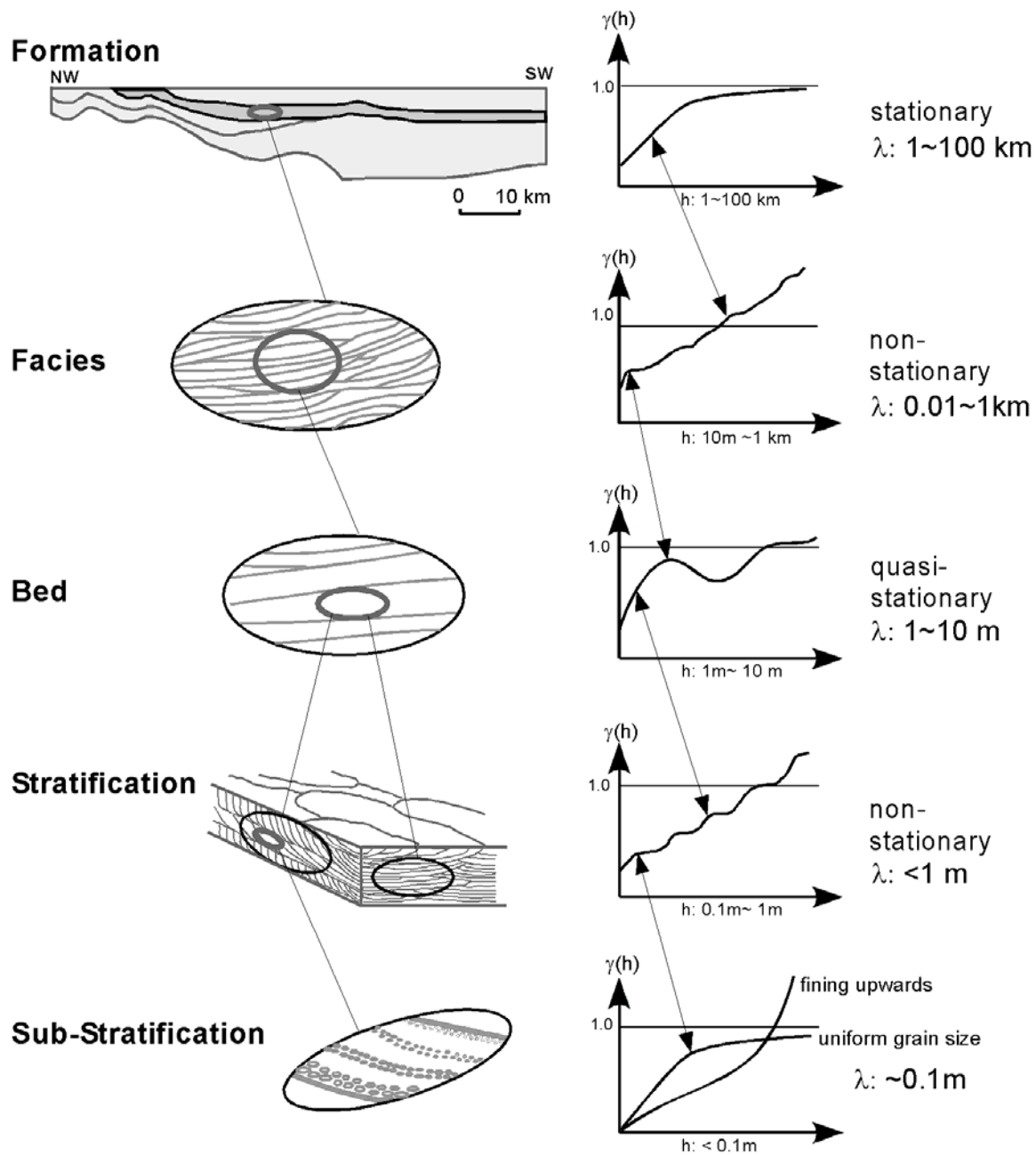


Figure 2. A schematic diagram showing the variogram structure as the scale of the problem increases in a hypothetical basin with 5 scales of sedimentary hierarchy. The sample domain is indicated with black outline with a gray bold circle indicating a sub-scale. The experimental (minor) variograms are normalized by the sample variance. λ is the correlation scale.

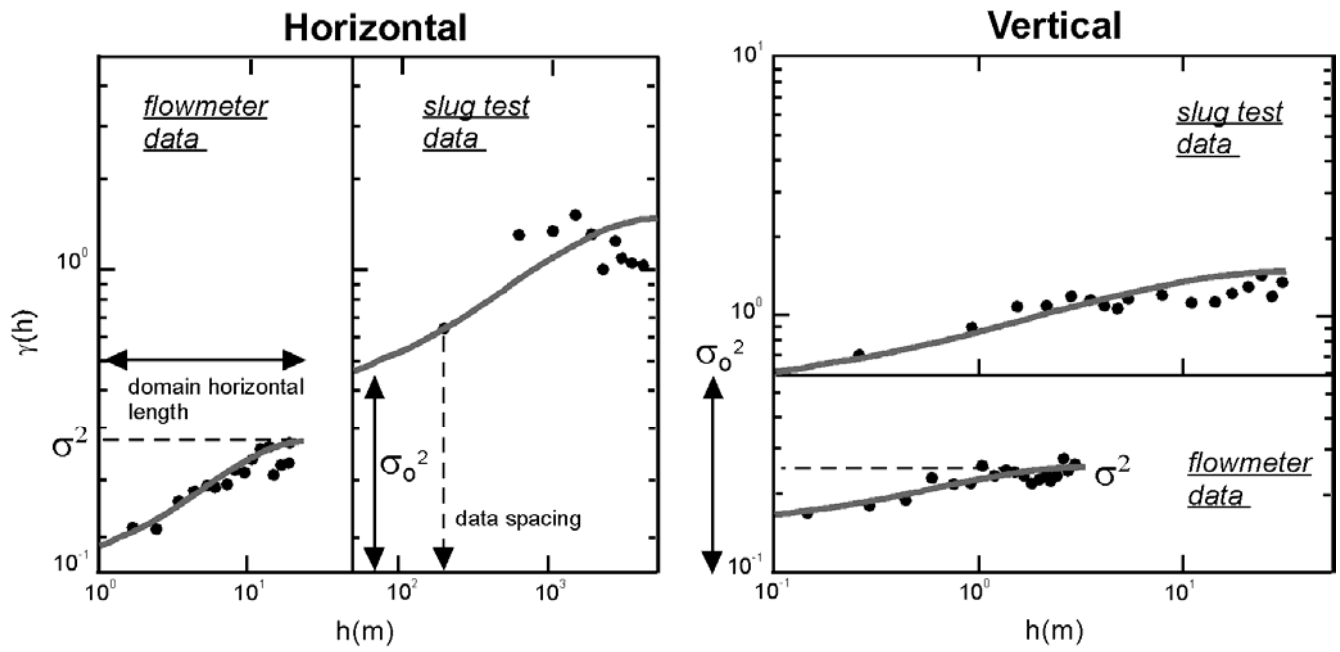
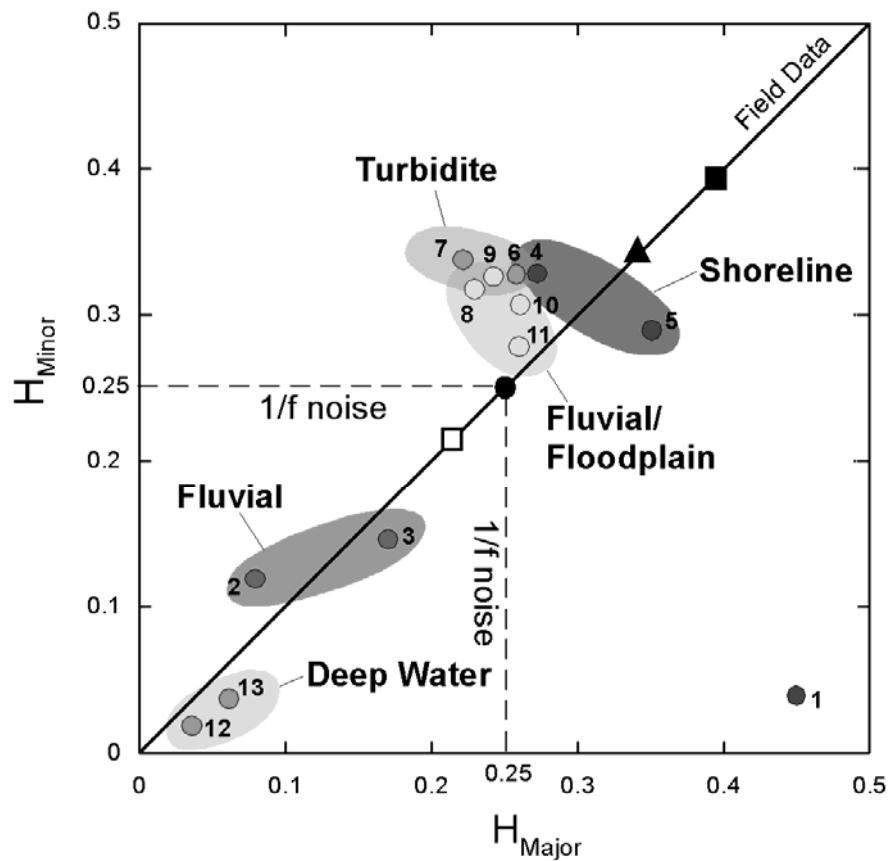


Figure 3. The Cape Cod experimental variograms (dots) re-interpreted. An exponential model (curves) is fitted onto each hierarchical variogram. σ^2 is the sill of the small sample from the flowmeter measurements; σ_o^2 is the nugget of the large sample from the slug test measurements.



sym.	H*	rock type	location	reference
□	0.22	sandstone	Alberta Basin	Desbarats and Bachu, 1994
▲	0.34	sandstone	Mobile, AB	Molz and Boman, 1995
■	0.39	fluvial sands	Savannah River site, SC	Liu and Molz, 1996
●	0.25	hypothetical "juxtaposition" of different media		Neuman (1990, 1994)

* estimated Hausdorff measure assuming self-affine fBm

Figure 4. A scatter plot of the Hausdorff measure estimated for each sample along the major (H_{Major}) and minor (H_{Minor}) directions. Sample ID is indicated along with the depositional environment. For comparison, Hausdorff measure obtained from field studies are also plotted along the 45° line.

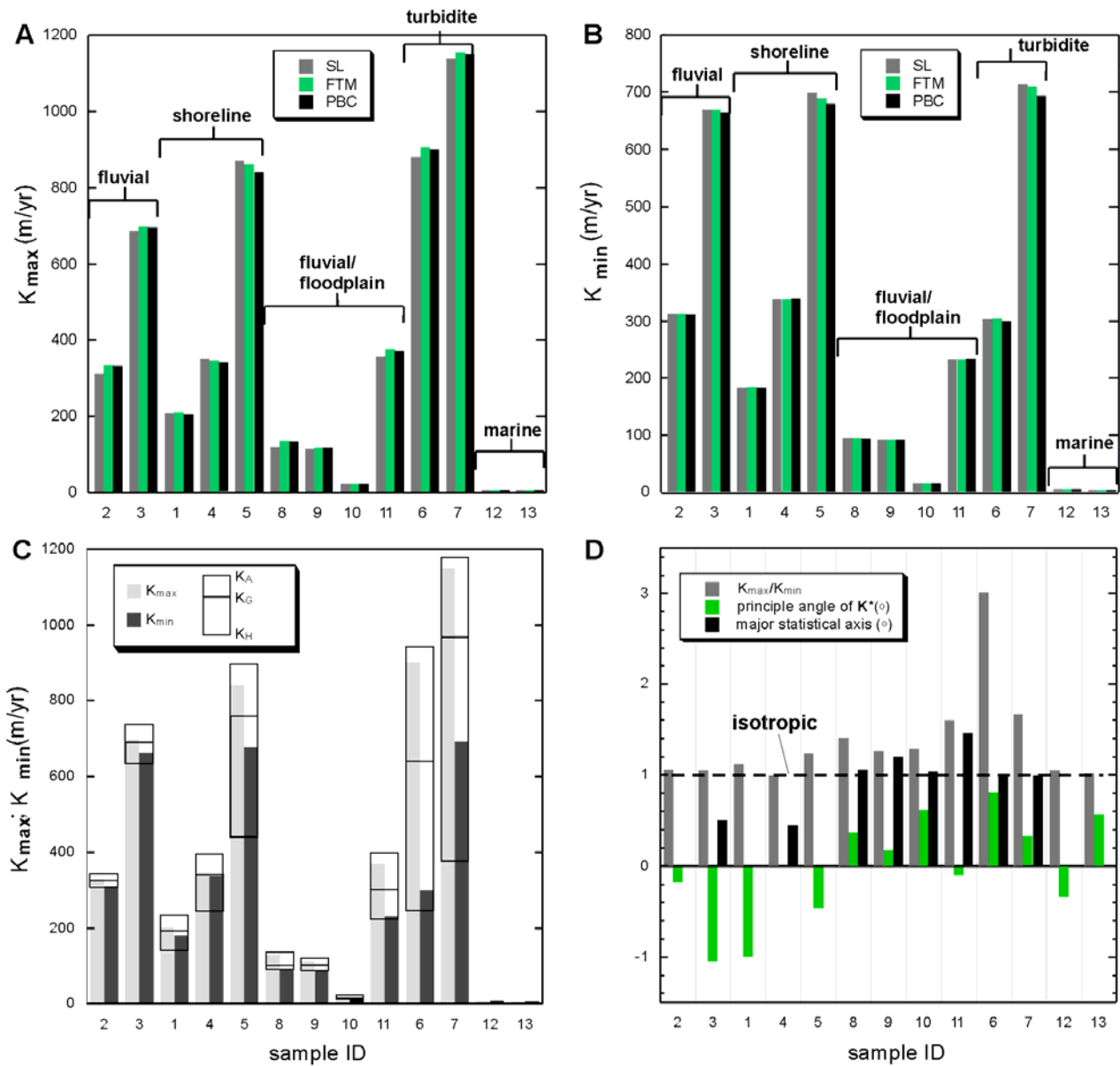


Figure 5. (A) The principal maximum conductivity (K_{max}) of K^* computed with SL, FTM, and PBC for 13 select samples. (B) The principal minimum conductivity (K_{min}) computed with these methods. (C) The principal components of K^* (PBC) plotted against the Wiener's bound: [K_H , K_A] and the geometric mean (K_G). (D) Using PBC, the global conductivity anisotropy ratio (K_{max}/K_{min}), the principal angle of K^* , and the major statistical axis (Zhang et al., 2004) are plotted. These angles are in degrees in reference to the horizontal axis.

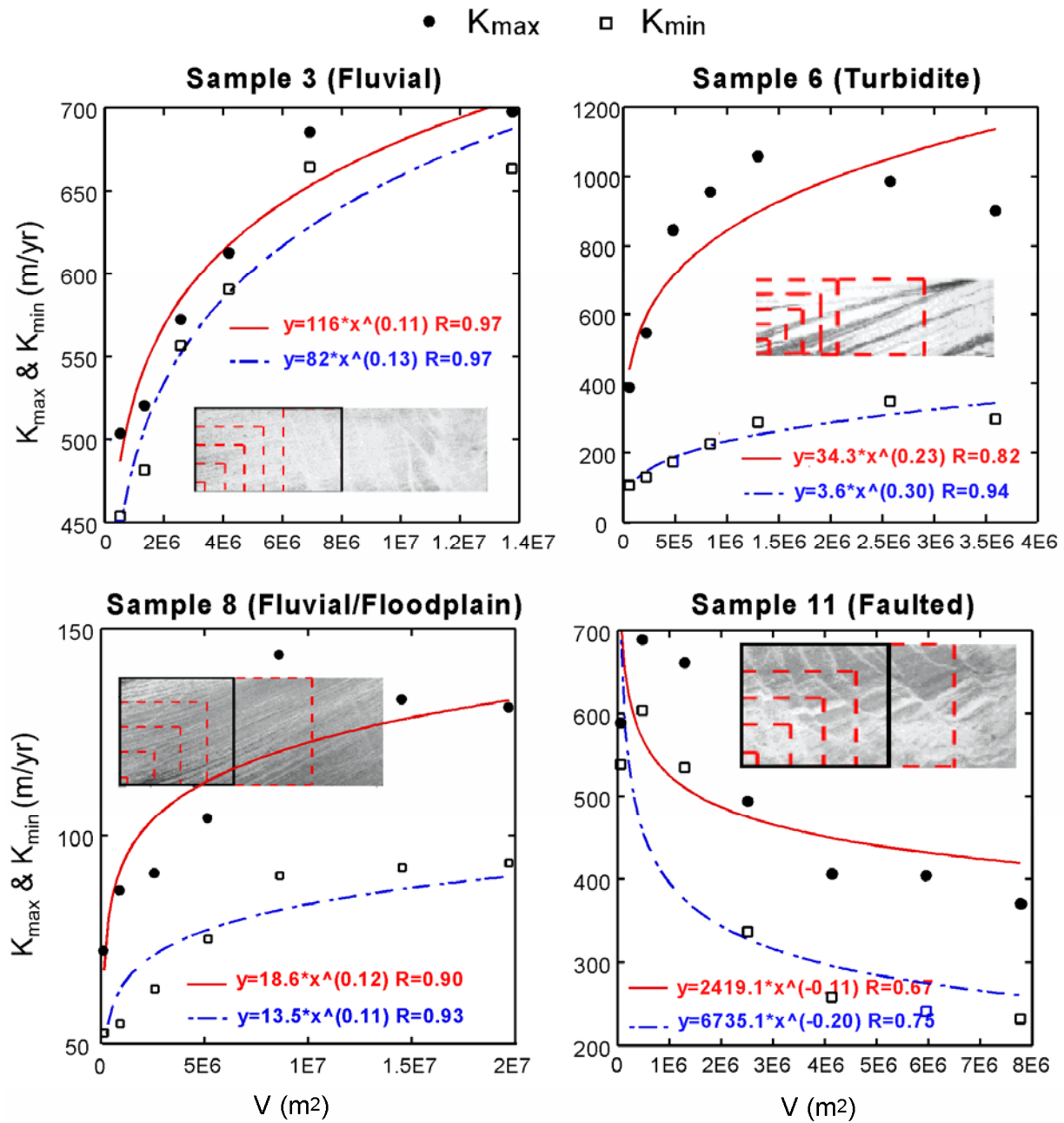


Figure 6. The principal components of K^* computed with PBC at different support sizes for the fluvial (sample 3), fluvial/ floodplain (sample 8), turbidite (sample 6), and faulted deposits (sample 11). The horizontal axis represents the area of each sub region selected for the up-scaling analysis. In each plot, the last data point corresponds to the full sample size: the bold outline indicates the size when an asymptotic K^* may be reached. A power law function is fitted onto each principal component; a scaling exponent is indicated in the fitted equation within a parenthesis.

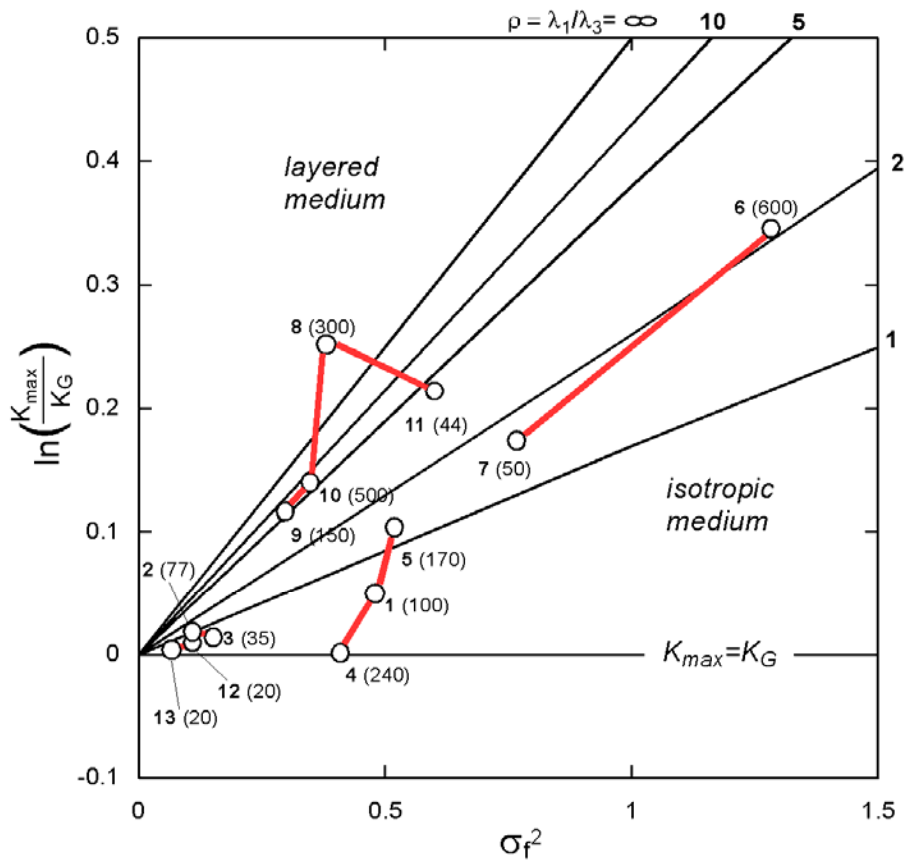


Figure 7. The natural log of (K_{\max}/K_G) verse $\ln K$ variance for 13 select samples (circles). K_{\max} is computed with the PBC, and the sample ID is bold along with the estimated statistical anisotropy ratio in parenthesis. The genetically related samples are further linked by bold lines. Also shown is the stochastic-analytic prediction for different statistical anisotropy ratio (lines).

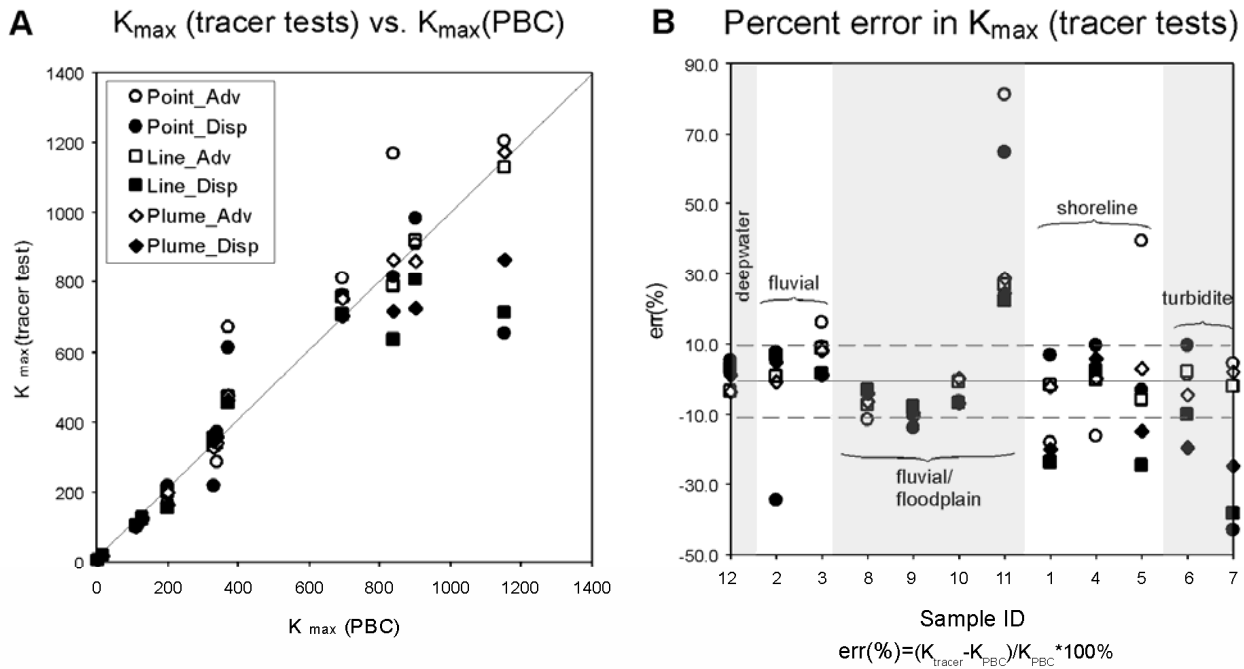


Figure 8. (A) A scatter plot of tracer test K_{\max} against that computed with PBC, arranged in increasing magnitude of K_{\max} for all samples. (B) Percent error in tracer test K_{\max} arranged in the order of the depositional environment. Note that all tests with local dispersion is represented with solid symbols.

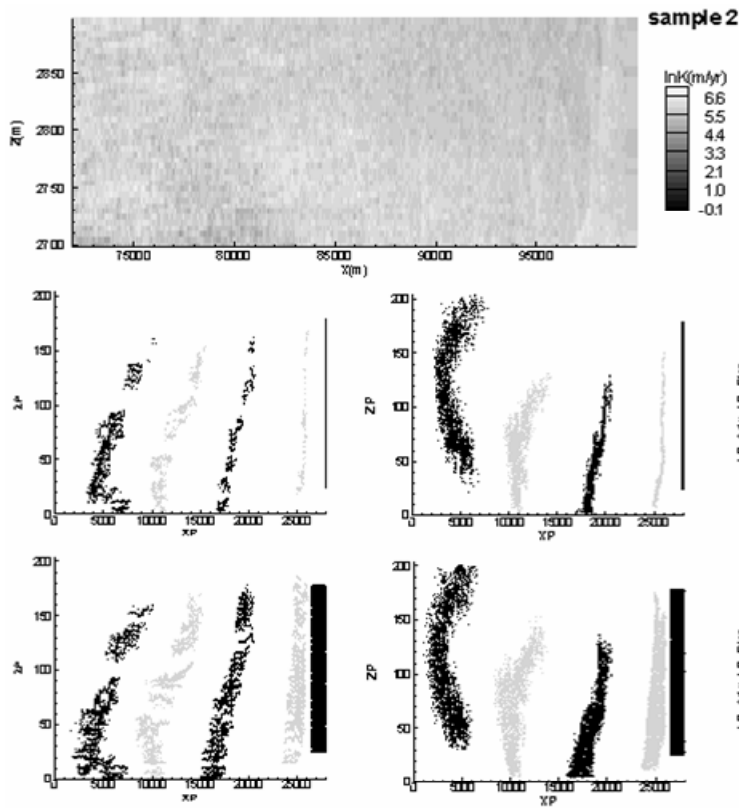


Figure 9. Sample 2 InK map, tracer tests of both a line source and a plume source, for a purely advective case and a case with local dispersion ($aL=10.0$ m, $aT=0.1$ m). For all four cases, the mean plume displacement over time is plotted as well as the apparent longitudinal macro-dispersivity over the mean displacement.

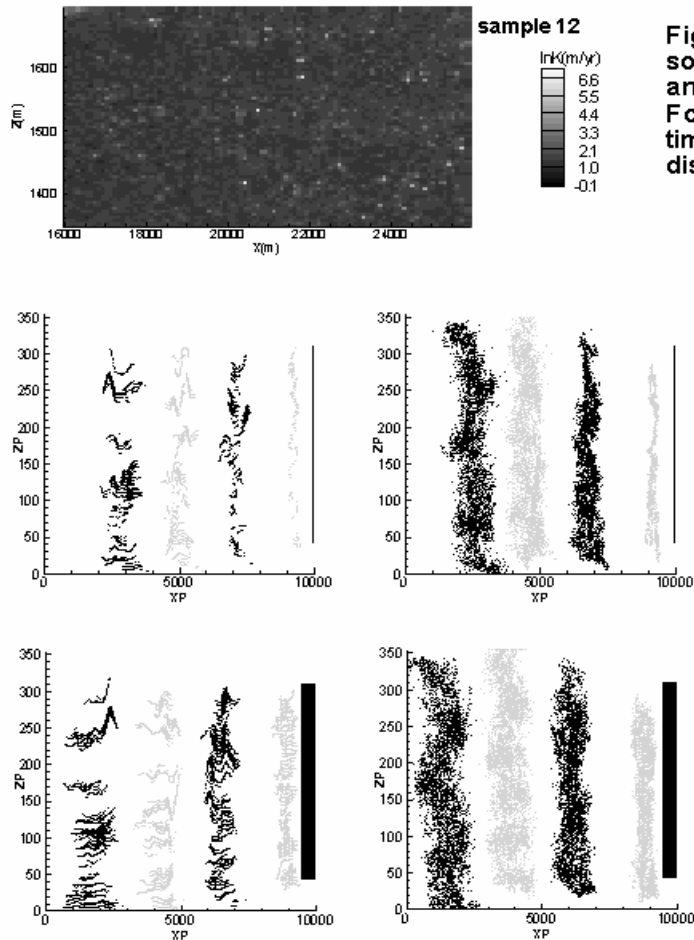


Figure 10. Sample 12 InK map, tracer tests of both a line source and a plume source, for a purely advective case and a case with local dispersion ($aL=10.0$ m, $aT=0.1$ m). For all four cases, the mean plume displacement over time is plotted as well as the apparent longitudinal macro-dispersivity over the mean displacement.

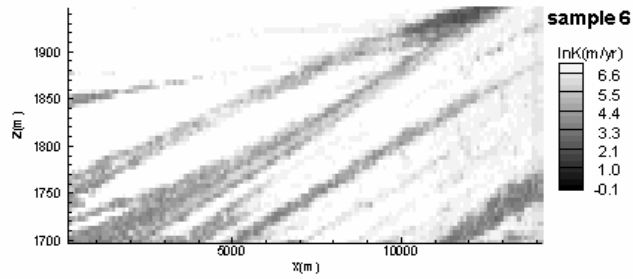
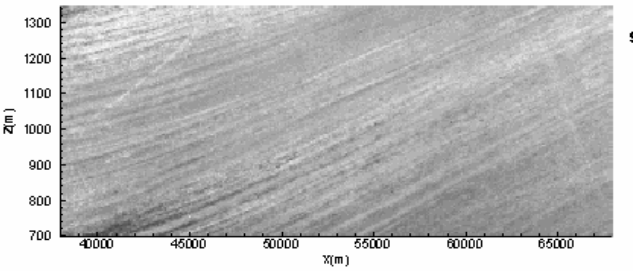
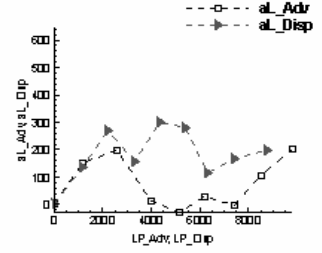
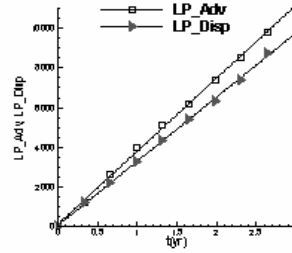
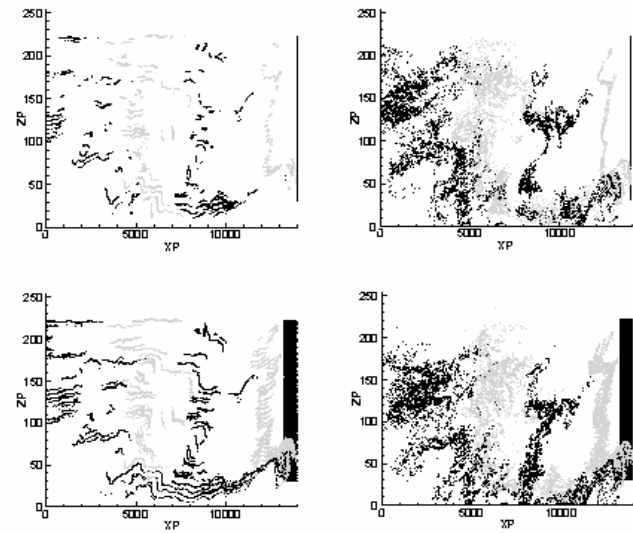
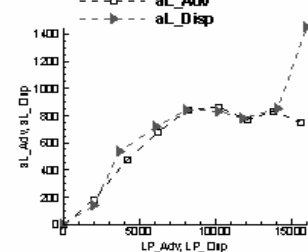
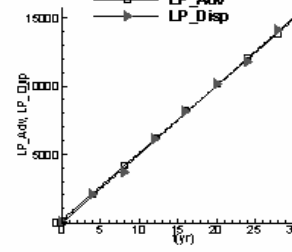
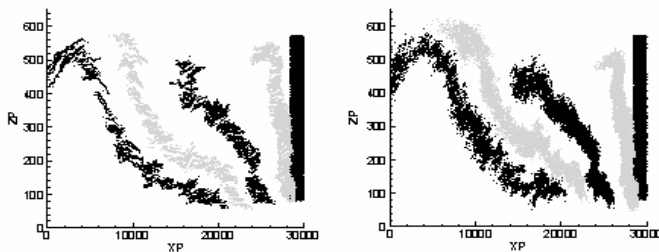
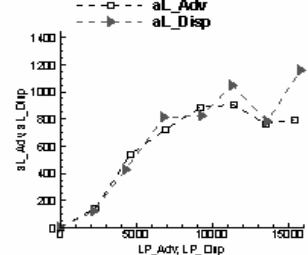
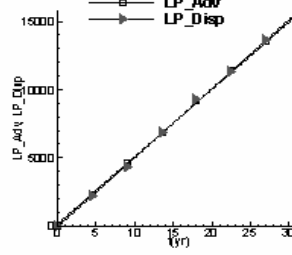
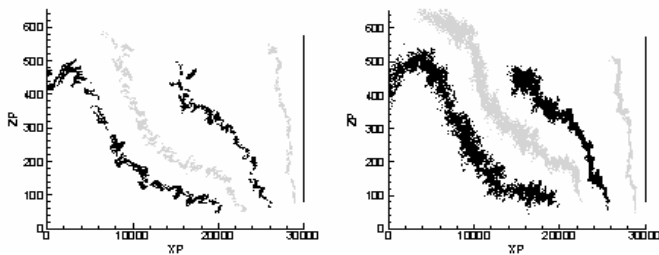


Figure 11. Sample 6 InK map, tracer tests of both a line source and a plume source, for a purely advective case and a case with local dispersion ($aL=10.0$ m, $aT=0.1$ m). For all four cases, the mean plume displacement over time is plotted as well as the apparent longitudinal macro-dispersivity over the mean displacement.



sample 8

Figure 12. Sample 8 InK map, tracer tests of both a linesource and a plume source, for a purely advective case and a case with local dispersion ($aL=10.0$ m, $aT=0.1$ m). For all four cases, the mean plume displacement over time is plotted as well as the apparent longitudinal macro-dispersivity over the mean displacement.



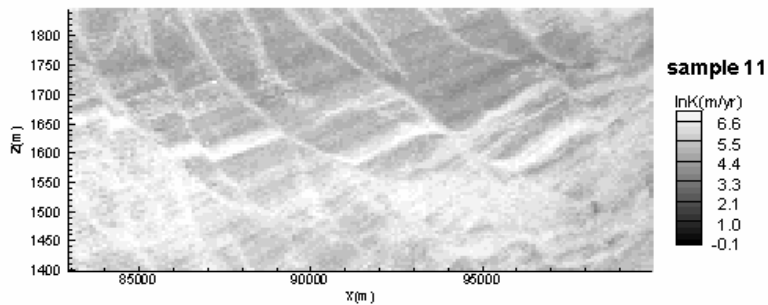
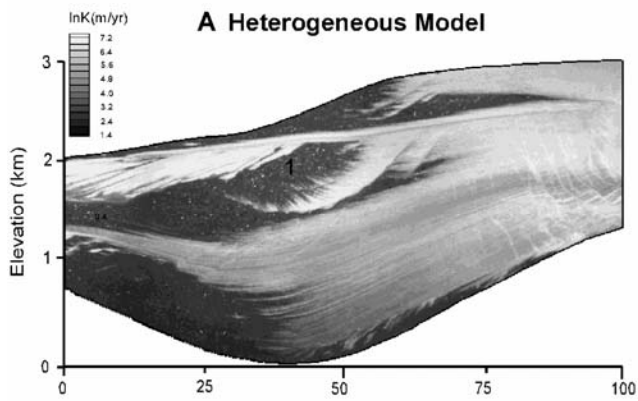
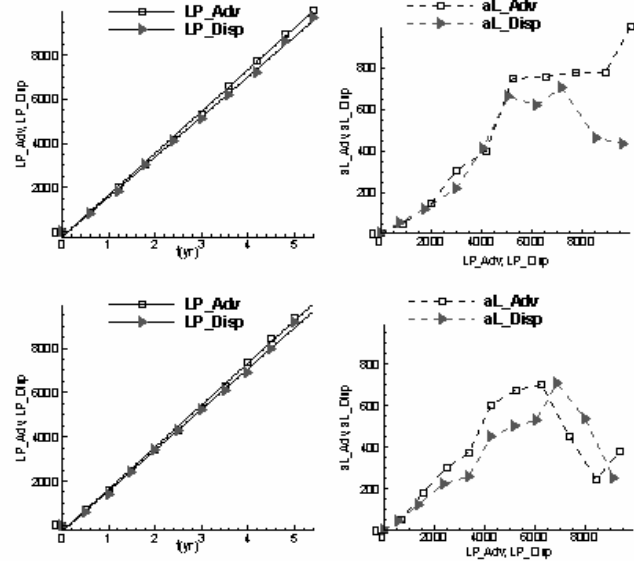
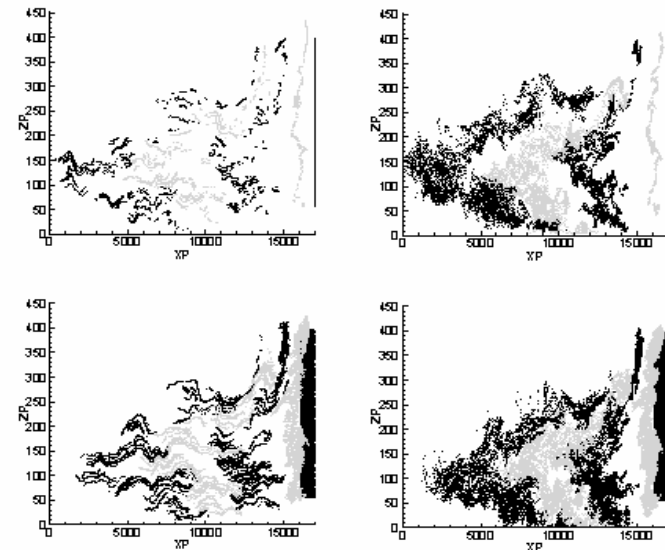


Figure 13. Sample 11 InK map, tracer tests of both a line source and a plume source, for a purely advective case and a case with local dispersion ($aL=10.0$ m, $aT=0.1$ m). For all four cases, the mean plume displacement over time is plotted as well as the apparent longitudinal macrodispersivity over the mean displacement.



B Hydro-stratigraphic Model

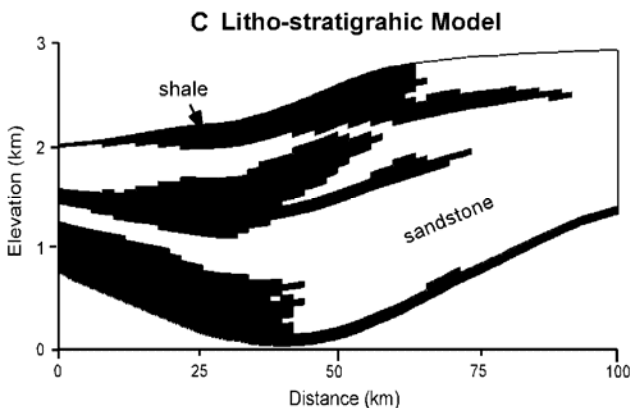
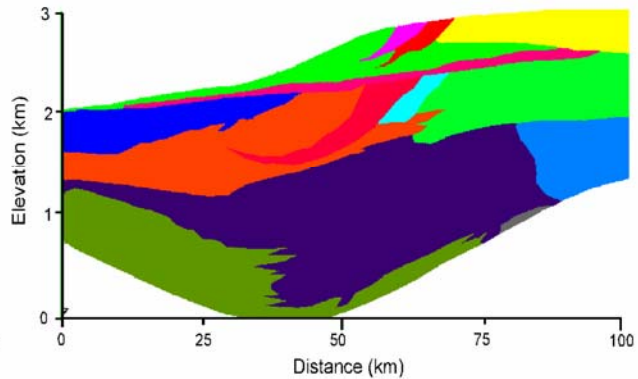


Figure 14. Three model representation of the basin-scale hydraulic conductivity map: (A) A complete distribution of the conductivity is represented by the fully heterogeneous model. (B) A hydro-stratigraphic model based on the geostatistical characteristics of the conductivity field. (C) A litho-stratigraphic model based on sand/clay cutoff.

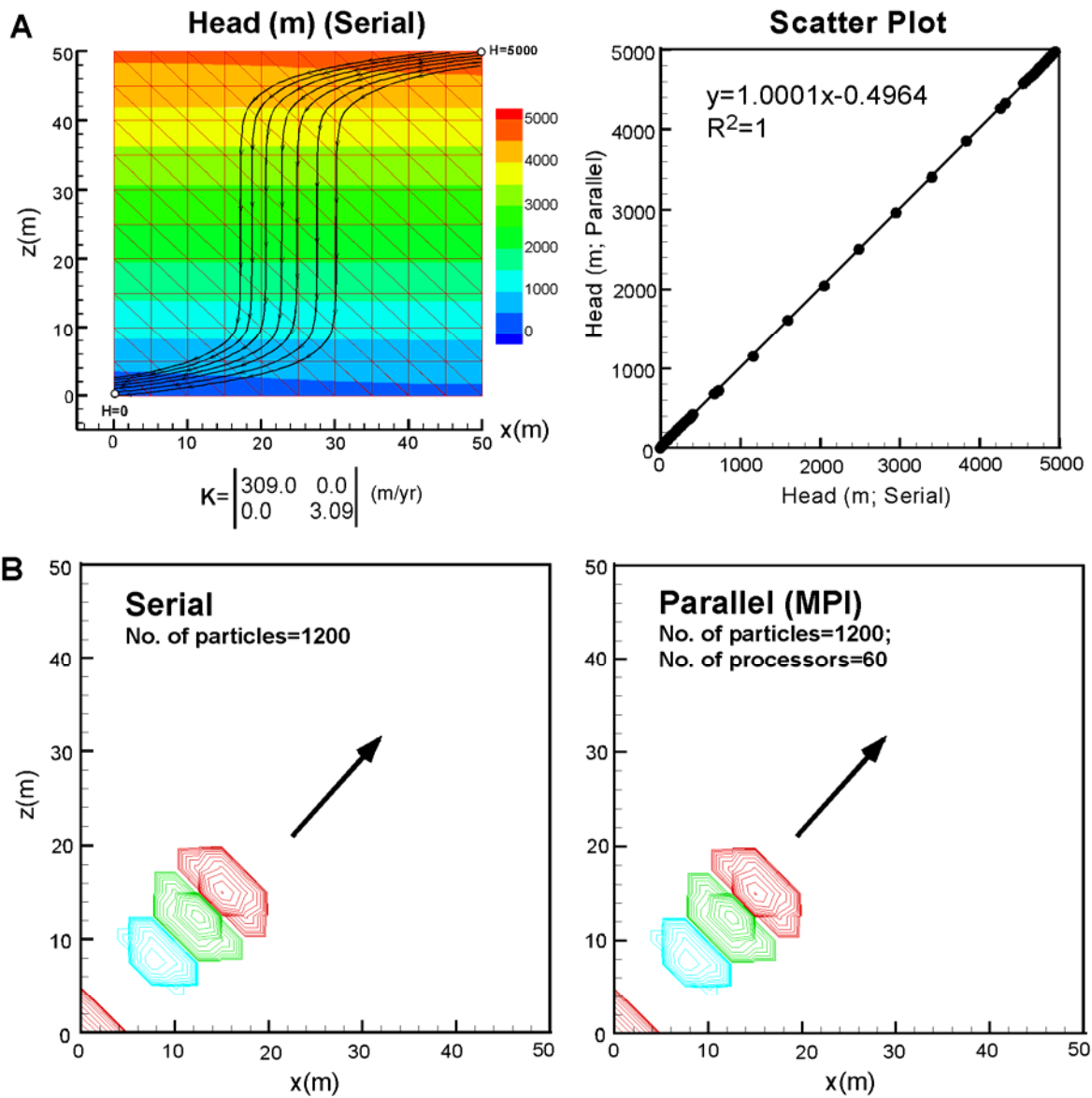


Figure 15. (A) The steady-state hydraulic head in a test flow problem solved with both serial and parallel codes. The serial solution is shown in a contour plot along with several trace lines of the velocity field. In the scatter plot, the serial solution is listed along the x-axis in the order of the nodes: 1, 2, ..., 121; the parallel solution is listed along the y-axis. (B) The solute concentration at 4 time steps solved using both a serial and parallel implementation of the RWPT method.

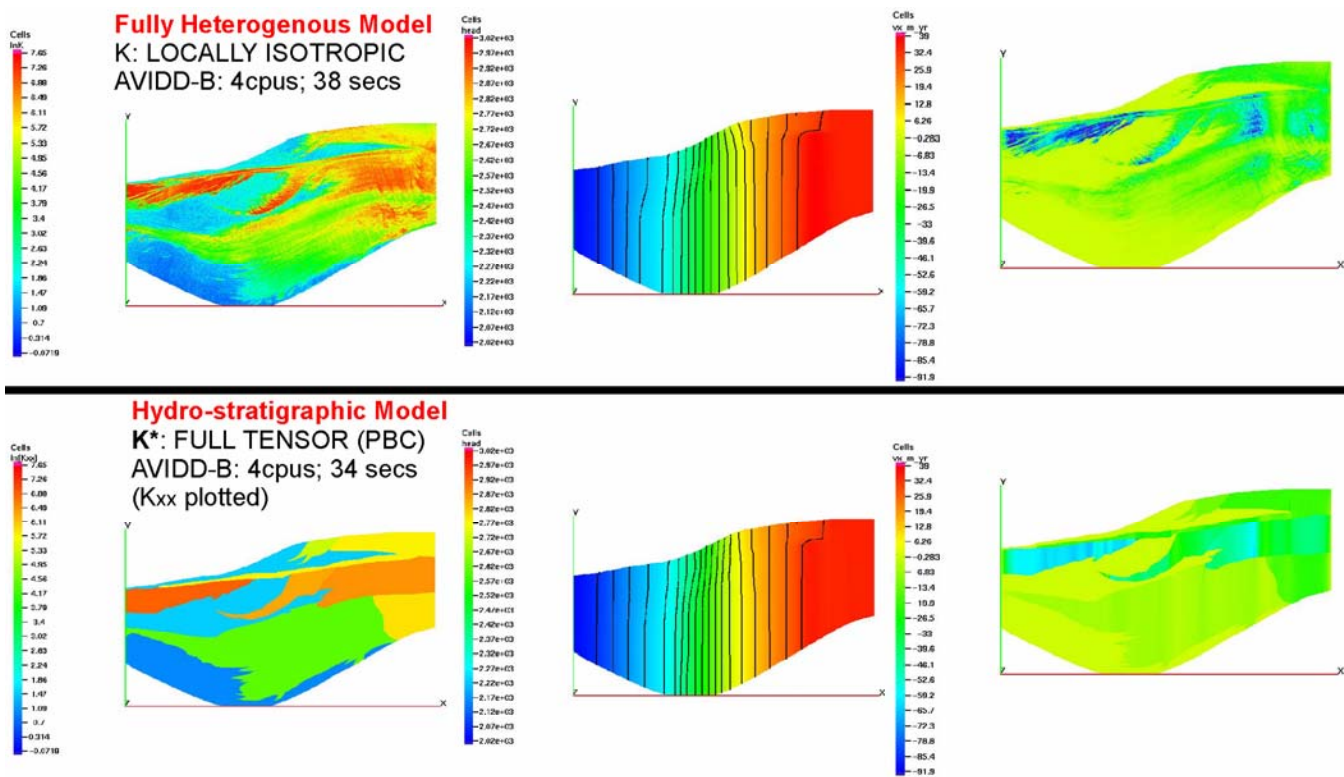
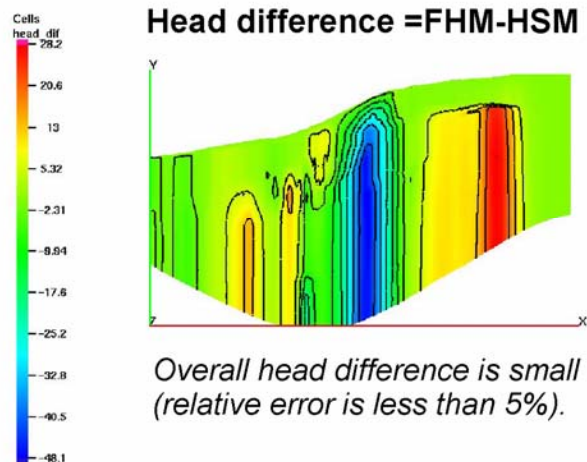


Figure 16. A preliminary full-basin flow simulation to compute the hydraulic head and groundwater velocity (shown is v_x) in the fully heterogenous model (FHM) and the hydro-stratigraphic model (HSM). Both models use the same grid to eliminate numerical errors due to grid coarsening.




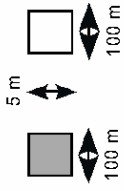
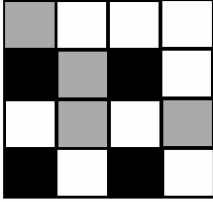
Scale	Conductivity	Dispersivity	Simulation
Pixel scale (scale of grain size in the deposits)		$\alpha_L < 10^{-3} \text{ m}$	none
Local scale (individual pixel scaled up)	 K (local K represents a homogeneous, isotropy porous medium)	$\alpha_L = 10^1 \text{ m}$ (local-scale dispersivity assigned based on Gelhar (1992), it represents solute dispersion due to sub-local scale conductivity heterogeneity not resolvable from the scaled-up	groundtruth heterogeneous model
Global scale (size of representative region for upscaling calculation; close to lithofacies scale)	 $K^* = \begin{bmatrix} K_{xx} & K_{xz} \\ K_{zx} & K_{zz} \end{bmatrix}$ (global K^* is an effective conductivity tensor for a representative region selected for upscaling; global K^* arises due to the spatial variations of the local scale K within this region.	α_L^M (macrodispersivity arises due to local-scale dispersivity α_L and conductivity heterogeneity)	lithofacies model (effective K^* for the litho-facies are obtained from upscaling of representative regions);

Table 1. Both the *scale-up* and *upscale* conducted in this study: scale-up is to transform a deposit-scale image (Figure 4) to a sedimentary basin and it occurs when each pixel at *pixel-scale* is transformed to a *local-scale* porous medium of dimension 100x5m. Correspondingly, the entire image has been “stretched” to a basin with a length of 100 km and average depth of 2 km. *Upscale* occurs when a global conductivity tensor K^* is computed from the local conductivity K distribution within a representative region of a lithofacies. Flow and transport simulations were conducted for the heterogeneous base model which utilize the local-scale K field and for the lithofacies model which utilize the global-scale K^* for each lithofacies. Note that globally (at the scale of the lithofacies), both the K^* and dispersivity arise as a result of local-scale conductivity heterogeneity.

Table 2. The geostatistical characteristics of lnK (m/yr) tabulated for the select samples as well as the effective hydraulic conductivity (K^*) (m/yr) estimated with three numerical methods and a stochastic-analytic model. For each sample, the associated depositional environment, sample variance (σ_p^2), the integral scales estimated along the major/minor statistical axes (λ_1 and λ_3), and the statistical anisotropy ratio (λ_1/λ_3) are listed. α is the angle of the major statistical axis with the horizontal plane. For each sample, K^* is computed with the SL, FTM and PBC. K^* computed with PBC has its principal components (K_{\max} , K_{\min}), the global anisotropy ratio ($Anis=K_{\max}/K_{\min}$) and the major axis (in relation to the horizontal plane) listed. The geometric mean of the local K is also listed as well as (K_{\max} , K_{\min}) estimated with Gelhar and Axness (1983). Compared to (K_{\max} , K_{\min}) estimated by the PBC, the relative error using the analytic model is also computed.

Sample ID	Depo. Environ.	σ_t^2	α (°)	λ_1 (m)	λ_3 (m)	λ_1/λ_3	Upscaled Global Tensor K^*						K^* (PBC)				K_G	Gelhar & Axness		relative err. (%)			
							SL		FTM		PBC		K_{max}	K_{min}	A_{anis}	θ (°)		K_{max}	K_{min}	K_{max}	K_{min}	max	min
1	shoreline	0.5	0	1000	10	100	205.7		208.4	0.3	202.4	-0.37		202.4	180.9	1.12	-1.0	192.5	243.8	192.5	17	6	
								180.6	-0.5	182.1	-0.4	180.9											
2	fluvial	0.1	0	517	7	78	309.5		331.7	-0.03	330.1	-0.08		330.1	311.2	1.06	-0.2	324.2	342.1	324.2	4	4	
								311.7	-0.04	312.2	-0.03	311.2											
3	fluvial	0.2	0.5	450	13	35	687.2		698.0	-1.0	697.0	-0.6		697.1	663.0	1.05	-1.0	687.9	739.0	547.6	6	-21	
								666.8	-0.6	666.5	-0.65	663.1											
4	shoreline	0.4	0.5	2400	10	240	348.5		343.1	0.7	339.1	0.35		339.3	338.5	1.00	0	339.0	415.5	271.5	18	-25	
								337.9	4.2	338.5	0.3	338.8											
5	shoreline	0.5	0	1700	10	170	872.0		861.9	0.3	840.8	-1.3		840.8	677.0	1.24	-0.4	757.0	979.4	757.0	14	11	
								696.9	0.7	686.5	-1.3	677.0											
6	turbidite	1.3	1	8000	13	600	880.7		905.4	7.4	900.8	8.5		901.0	298.9	3.01	0.8	637.8	1207.6	387.9	25	23	
								303.2	9.2	303.9	8.6	299.0											
7	turbidite	0.8	1	700	14	50	1140.6		1155.4	3.1	1151.4	2.5		1151.4	691.1	1.67	0.3	965.8	1402.7	604.0	18	-14	
								711.2	12.9	707.3	2.5	691.1											
8	fluv./fld.	0.4	1	1500	5	300	115.7		131.7	0.4	130.8	0.2		130.8	93.0	1.41	0.4	101.6	122.8	60.7	-7	-53	
								93.5	0.3	93.7	0.25	93.0											
9	fluv./fld.	0.3	1.2	1500	10	150	110.9		114.1	0.06	114.1	0.07		114.1	90.6	1.26	0.2	101.6	117.9	56.5	3	-60	
								89.9	0.01	90.4	0.08	90.6											
10	fluv./fld. distal	0.4	1	3500	7	500	19.0		19.5	0.04	19.5	0.05		19.5	15.1	1.29	0.6	16.9	20.1	10.1	3	-50	
								15.0	0.06	15.1	0.05	15.1											
11	faulted fluv./fld.	0.6	1.5	883	20	44	354.8		372.5	-0.6	370.3	-0.2		370.3	231.6	1.60	-0.1	299.2	399.8	151.7	7	-53	
								230.6	-0.5	231.4	-0.2	231.6											
12	marine	0.1	0	120	6	20	4.5		4.6	0.0	4.56	0.0		4.6	4.4	1.05	-0.3	4.5	4.8	4.5	4	4	
								4.3	0.0	4.4	0.0	4.35											
13	marine	0.1	0	130	7	20	2.7		2.8	0.0	2.8	0.0		2.8	2.7	1.02	0.6	2.8	2.8	2.8	3	2	
								2.7	0.0	2.7	0.0	2.7											

Table 3. The effective hydraulic conductivity K^* (m/yr) of the fluvial/floodplain deposits (sample 8, 9, 10) computed with PBC and a stochastic-analytic model (Gelhar and Axness, 1983). Two different exponential variogram models are fitted onto the minor variograms of these deposits: a small scale model fitting only the first sill; a larger scale model fitting to a higher, global sill assuming that a larger scale statistical homogeneity exists.

ID	σ^2_f	λ_{max}	PBC				small scale model						larger scale model					
									Stocha.-Ana.		error (%)				Stocha.-Ana.		error (%)	
			K^*		K_{max}	K_{min}	λ_3	λ_1/λ_3	K_{max}	K_{min}	K_{max}	K_{min}	λ_3	λ_1/λ_3	K_{max}	K_{min}	K_{max}	K_{min}
8	0.38	1500	130.81 0.25	0.24 93.04	130.8	93.04	5	300	122.8	60.7	-6.6	-53.2	500	3	114.6	88.3	-14.1	-5.4
9	0.30	1500	114.1 0.08	0.07 90.58	114.1	90.58	10	150	117.9	56.5	3.2	-60.4	500	3	111.8	86.4	-2.1	-4.9
10	0.35	3500	19.46 0.05	0.05 15.10	19.46	15.10	7	500	20.1	10.1	3.4	-49.6	650	5.4	19.3	12.8	-0.6	-17.5

Table 4. K_{max} estimated via tracer tests using different tracer dimensions, with or without representing local dispersion. K_{max} computed using PBC is listed for comparison. The estimation discrepancy is defined as $err(\%) = (K_{tracer} - K_{PBC}) / K_{PBC} * 100\%$. For each sample, the best and the worst estimates are in bold and italic, respectively.

Depo. Environ.	Sam ID	Point Source				Line Source				Plume				PBC
		Adv.		Disp.		Adv.		Disp.		Adv.		Disp.		
		K _{max}	err (%)	K _{max}	err (%)	K _{max}	err (%)	K _{max}	err (%)	K _{max}	err (%)	K _{max}	err (%)	
Shoreline	1	165.8	-18.1	216.0	6.7	199.0	-1.7	154.6	-23.6	198.0	-2.2	162.1	-19.9	202.4
	4	284.4	-16.2	371.9	9.6	337.7	-0.5	348.0	2.6	340.2	0.3	358.8	5.7	339.3
	5	1770.3	39.2	815.6	-3.0	789.6	-6.1	632.2	-24.8	864.9	2.9	716.7	-14.8	840.8
Upstream Fluvial	2	355.0	7.6	276.0	-34.5	331.8	0.5	352.4	6.8	327.3	-0.8	345.6	4.7	330.0
	3	808.9	16.1	760.6	9.1	756.4	8.5	707.3	1.5	752.4	7.9	703.2	0.9	697.0
Turbidite	6	911.4	1.2	984.8	9.3	920.1	2.1	807.4	-10.4	859.3	-4.6	724.0	-19.6	901.0
	7	1203.4	4.5	654.0	-43.2	1126.4	-2.2	710.9	-38.3	1174.7	2.0	865.6	-24.8	1151.4
Fluvial/ Floodplain	8	775.7	-11.5	121.7	-7.0	120.8	-7.6	126.3	-3.4	122.5	-6.3	125.6	-4.0	130.8
	9	98.0	-14.1	98.1	-14.0	104.7	-8.2	105.3	-7.7	101.8	-10.8	103.0	-9.7	114.1
	10	18.2	-6.5	78.7	-7.0	19.3	-0.8	18.1	-7.0	19.5	0.2	18.1	-7.0	19.5
	11	677.2	81.3	610.6	64.9	469.1	26.7	452.5	22.2	475.9	28.5	460.3	24.3	370.3
Deep Water	12	4.4	-3.5	4.8	5.3	4.4	-3.5	4.7	3.1	4.4	-3.5	4.6	0.9	4.6